

ARTICLE OPEN



High-throughput screening of room temperature active Peltier cooling materials in Heusler compounds

Huifang Luo¹, Xin Li^{1,2}✉, Yuxiang Wang¹, Yeqing Jin¹, Mingjia Yao¹ and Jiong Yang^{1,3}✉

Active Peltier cooling enables Peltier heat transfer in addition to the traditional Fourier thermal conductance, which is useful in some special applications, such as the microthermostats. From the material wise, however, the study on the active Peltier cooling materials is rare. We carried out a high-throughput workflow to screen out 5 room-temperature active Peltier cooling materials, GaSbLi₂, HgPbCa₂, SnTiRu₂, GeYbLi₂, and GeTiFe₂, from 2958 Heusler materials. All the five materials are semimetals or very narrow band gap systems with high electrical conductivity. Some of these materials have relatively large Seebeck coefficients due to the band asymmetry. Their effective thermal conductivity K_{eff} s, which are the summation of active Peltier thermal conductivity and passive thermal conductivity, are all greater than Cu at the room temperature and $\Delta T = 1$ K. The present work gives a possible way to search active cooling Peltier materials for the applications of precise temperature control.

npj Computational Materials (2022)8:199; <https://doi.org/10.1038/s41524-022-00887-4>

INTRODUCTION

Active Peltier cooling materials can accelerate heat transfer by consuming electric energy, which have applications in integrated circuit chip cooling, lithium-ion batteries, microthermostat, medical temperature controlling, etc^{1–4}. With the development of batteries and computer chips toward more compact and higher power density, these applications require more sophisticated thermal management techniques, and thermal flow management becomes increasingly important^{5–7}. From the application of the active cooling material mentioned above, its operating temperature is general around the room temperature. Figure 1 is a schematic diagram of active cooling. T_H is the temperature of the heat source, Q_p and Q_f are the heat pumped by the work done through the Peltier effect and Fourier effect, respectively. The current I_s passes through the p-n leg to pump heat from the hot end to the ambient temperature. The main parameter for assessing the performance of active cooling materials is the effective thermal conductivity K_{eff} ⁸

$$K_{eff} = K_{pas} + K_{ac} = K_{pas} + \frac{PF \cdot T_H^2}{2\Delta T}, \quad (1)$$

where K_{pas} is the passive thermal conductivity (including the electronic thermal conductivity κ_e and lattice thermal conductivity κ_l) affected by the Fourier effect, and K_{ac} is the active thermal conductivity affected by the Peltier effect. ΔT is the temperature difference of the hot source and room temperature. Power factor ($PF = S^2\sigma$) is composed of the Seebeck coefficient S and the electrical conductivity σ . Materials with high power factor and high passive thermal conductivity are required to quickly and effectively remove heat from the hot region of the device^{8–10}.

Generally speaking, metals with large κ_e dominate the passive cooling applications^{11,12}. As for active cooling, however, metals generally have small Seebeck coefficients and therefore small PF s, so currently only some metals with strong localized f electrons have been considered in active cooling applications⁸.

Most of the thermoelectric semiconductors with large PF s, on the other hand, have the best working temperature range far above 300 K^{13–17}, which is not applicable to the desired working temperature of active cooling. As for some room temperature thermoelectric materials such as Bi₂Te₃^{18,19}, due to their low κ_l s, the K_{eff} s are far below the passive thermal conductivity of Cu at the room temperature. Therefore, conventional metals and thermoelectric semiconductors are not suitable for active cooling.

Semimetals naturally have large electrical conductivity σ as well as thermal conductivity κ ²⁰, and they are potentially good active cooling materials. Semimetals have zero band gap with E_F usually passing through conduction band minimum (CBM) or valence band maximum (VBM) or both, and their Seebeck coefficients are generally small. However, Markov et al. proposed that if semimetal materials have great asymmetry between conduction band and valence band, it is possible for them to have large Seebeck coefficients²¹. Therefore, semimetals with energy band asymmetry may be an option for room-temperature active cooling application.

Heusler alloys (including half-Heusler and full-Heusler) are a class of materials worthy of systematic study due to their wide variety of compositions and functional properties. Although there are many studies on Heusler alloys^{22–31}, room temperature active cooling application in these compounds has never been discussed. In this work, based on the MatHub-3d database^{32,33}, the Heusler alloys are systematically screened for room temperature active cooling in a high-throughput (HTP) manner. Within all the 2958 Heusler entries in the database (274 half-Heusler and 2684 full-Heusler), most of them have the band gaps lower than 0.1 eV, which are able to be treated as semimetal (or very narrow band-gap) systems mentioned above. After the evaluations of electronic structures, electrical and thermal transport properties, five Heusler materials with large effective thermal conductivity (K_{eff} at room temperature is greater than that of Cu at $\Delta T = 1$ K) were found, which are GaSbLi₂, HgPbCa₂, SnTiRu₂, GeYbLi₂, and GeTiFe₂. The asymmetry of electronic density of states (DOS) and/or electronic group

¹Materials Genome Institute, Shanghai University, Shanghai 200444, China. ²State Key Laboratory of Functional Materials for Informatics, Shanghai Institute of Microsystem and Information Technology, Chinese Academy of Sciences, Shanghai 200050, China. ³Zhejiang Laboratory, Hangzhou, Zhejiang 311100, China. ✉email: xinli@mail.sim.ac.cn; jiong.yang@shu.edu.cn

velocities are responsible for the large k_{eff} in these Heusler compounds. This work provides strategies and material systems for the active Peltier cooling application.

RESULTS

Figure 2a shows the crystal structures of half-Heusler compound ABX and full-Heusler compound AB₂X. Elements A and X form a rock-salt structure. For half-Heusler, element B locates at one of the two body diagonal position (1/4, 1/4, 1/4) in the cell. When the other body diagonal position (3/4, 3/4, 3/4) is also occupied, it becomes the structure of full-Heusler. In the repository MatHub-3d, there are 274 half-Heusler entries (under the search criteria of space group No. 216, atomic ratio as 1:1:1), and 2684 full-Heusler entries (under the search criteria of space group No. 225, atomic ratio as 1:2:1). For the HTP study in this work, in order to obtain a relatively better description of the band structures for Heusler alloys, the SCAN semilocal functional was adopted, as mentioned in the Methods section.

To effectively screen the active Peltier cooling materials in Heusler alloys, we designed the workflow as shown in Fig. 2b. As discussed

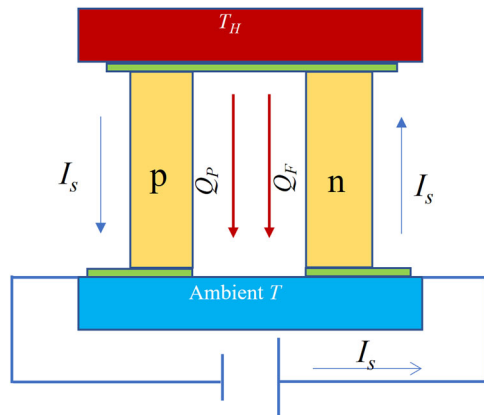


Fig. 1 Schematic diagram of active cooling. The current I_s pumps heat from the hot end to the ambient temperature through the p-n leg. Q_p and Q_F are the heat extracted by the Peltier effect and Fourier effect, respectively.

before, we eliminated those entries with $E_g \geq 0.1$ eV under the SCAN level, and obtained 122 half-Heusler and 2641 full-Heusler alloys as potential semimetal or very narrow band-gap entries. The electrical transport properties of these systems are then calculated under the CEPCA with the DOS-influenced relaxation time considered (Eq. 6). And Seebeck coefficients are independent with the electron-phonon coupling parameters under this method³⁴. Both the p-type and n-type Pisarenko curves for all the 2763 entries at 300 K are calculated, which can be found at the database of Mathub-3d (<http://www.mathub3d.net/static/database/Seebeckdata.zip>). Taking the Ioffe's criterion for potentially good candidates with high PFs, i.e., $|S| \geq 180 \mu\text{V K}^{-1}$ ³⁵⁻³⁷ for either p-type and n-type transport properties, 12 half-Heusler, and 7 full-Heusler entries are screened.

Due to the fact that some of these 19 systems have heavy elements with strong spin-orbital coupling (SOC), the SCAN+SOC electronic structures are further carried out. The deformation potentials and Young's moduli, which are needed for the relaxation times under the deformation potential method (Eq. 6), are also calculated, and the absolute values of power factors can be obtained. Combining the room temperature maximum PFs (PF_{max}) at the band edge³³ and κ_{LS} (Eq. 7), the k_{eff} vs ΔT (from 1 K to 10 K) for the 19 systems at $T_H = 300$ K are plotted in Supplementary Fig. 1. Five full-Heusler alloys with k_{eff} under either carrier type larger than κ_{Cu} (400 W mK^{-1} at 300 K)³⁸ are finally obtained under $\Delta T = 1$ K. Supplementary Table 1 in the supplemental material shows the values of c_{11} , c_{12} and c_{44} for GaSbLi₂, HgPbCa₂, SnTiRu₂, GeYbLi₂, and GeTiFe₂. According to the Born-Huang stability criterion ($c_{44} > 0$, $c_{11} - c_{12} > 0$, and $c_{11} + 2c_{12} > 0$), the five screened potential Heusler alloys are all thermally stable³⁹.

Table 1 lists the key parameters for the five compounds, including the E_{def} s, G s, S_{max} s, PF_{max} s, κ_{LS} , the electron group velocity v_{eS} , carrier concentration n_s , and electrical conductivity σ . The carrier concentration, S_{max} and v_e are corresponding to the PF_{max} . All the transport properties in Table 1 are the values at 300 K. Except for GaSbLi₂, all the other four compounds have better n-type electrical transport performance than p-type.

Figure 3 shows the active cooling performance of the five screened compounds in their favorable carrier types at the room temperature, with ΔT in the range of 1 K-10 K. The experimental k_{eff} s of the metals Co and CePd₃ are also labeled in Fig. 3. According to Eq. 1, the k_{eff} decreases with increasing temperature difference. When $\Delta T = 1$ K, the k_{eff} s of all the five compounds are

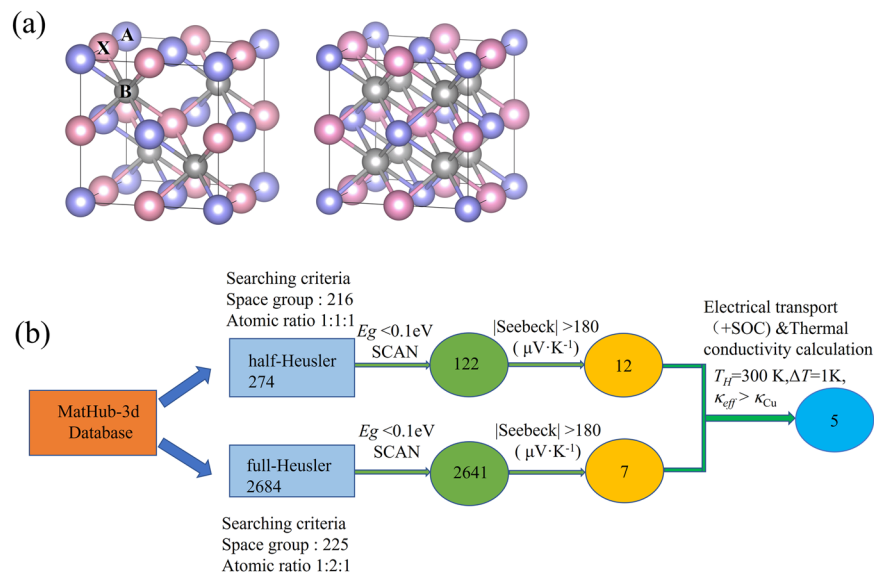


Fig. 2 High-throughput workflow of screening Heusler systems in active cooling application. **a** The crystal structures of half-Heusler and full-Heusler alloys. **b** The workflow of the present work.

Table 1. Parameters of five screened Heusler systems for active cooling application.

System	Type	E_{def} (eV)	G (GPa)	S_{max} ($\mu\text{V K}^{-1}$)	PF_{max} (10^{-4}W mK^{-2})	κ_L (W mK^{-1})	v_e (m s^{-1})	n (10^{20}cm^{-3})	σ (S m^{-1})
GaSbLi ₂	n-type	2.98	73	-64	201	18.6	612,000	19.85	4,970,000
	p-type	2.98		66	266		613,000	28.32	6,120,000
HgPbCa ₂	n-type	3.55	62	-136	115	6.6	321,000	6.87	621,000
	p-type	3.54		98	44		509,000	2.74	453,000
SnTiRu ₂	n-type	1.43	275	-147	301	30.2	149,000	6.99	1,390,000
	p-type	1.42		43	127		565,000	3.69	6,680,000
GeYbLi ₂	n-type	2.58	74	-160	143	11.6	217,000	2.88	552,000
	p-type	2.90		64	43		661,000	1.41	1,050,000
GeTiFe ₂	n-type	1.72	316	-157	220	47.6	121,000	9.53	888,000
	p-type	2.91		31	41		175,000	72.18	4,180,000

Deformation potential (E_{def}), Young's modulus (G), Seebeck coefficient with the carrier concentration of maximum power factor (S_{max}), the maximum power factor (PF_{max}), lattice thermal conductivity (κ_L), electron group velocity (v_e), carrier concentration (n), and electrical conductivity (σ) for GaSbLi₂, HgPbCa₂, SnTiRu₂, GeYbLi₂, and GeTiFe₂. Both n-type and p-type are included.

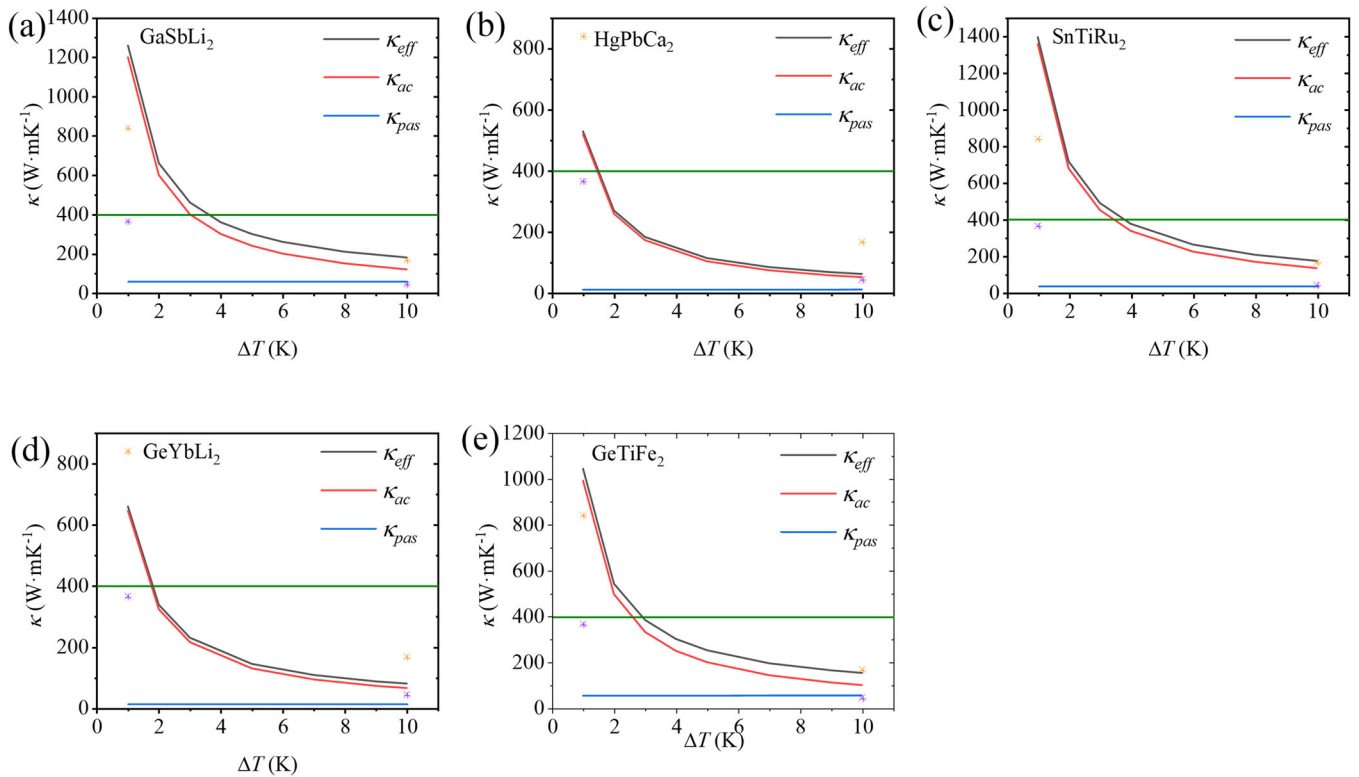


Fig. 3 Effective thermal conductivities with $\Delta T = 1\text{ K}–10\text{ K}$. **a** GaSbLi₂ **b** HgPbCa₂ **c** SnTiRu₂ **d** GeYbLi₂ **e** GeTiFe₂. In each plot, the black line represents κ_{eff} , the red line κ_{ac} , the blue line κ_{pas} , and the green line represents the thermal conductivity of Cu at room temperature. The orange and purple asterisks represent the effective thermal conductivity of Co and CePd₃ at $\Delta T = 1\text{ K}$ ⁸, respectively.

greater than that of Cu at 300 K, and the κ_{eff} s of GaSbLi₂, SnTiRu₂, and GeTiFe₂ are even greater than that of Co and CePd₃⁸. However, when $\Delta T \geq 5\text{ K}$, the κ_{eff} s of all the compounds are lower than the passive thermal conductivity of Cu, indicating that the applications of the active cooling only dominate at small temperature difference, such as in the precise temperature control. Figure 3 also shows that the contribution of PF-induced κ_{ac} plays a leading role comparing with the passive thermal conductivity when ΔT is small. For the future material selection for active cooling, the fact that PF dominates κ_{eff} indicates that it is not necessary to search compounds within metals or semimetals; any material with large power factor, e.g., $89 \times 10^{-4}\text{ W mK}^{-2}$, will

have a better κ_{eff} than that of Cu at room temperature with $\Delta T = 1\text{ K}$, without even considering the contribution of κ_{pas} .

DISCUSSION

The very high PFs of the five compounds are the underlying reason for their large κ_{ac} , which can be rationalized by the band asymmetry. Figure 4 shows the band structures and DOS of (a) SnTiRu₂ (b) GeYbLi₂ (c) GeTiFe₂ (d) HgPbCa₂ (e) GaSbLi₂. For SnTiRu₂, GeYbLi₂, GeTiFe₂, HgPbCa₂ full-Heusler, there is a large band asymmetry with larger DOS at CBM. We define $N(\epsilon_F + \epsilon)/N(\epsilon_F - \epsilon)$ or $N(\epsilon_F - \epsilon)/N(\epsilon_F + \epsilon)$ as the DOS asymmetry ratio at the same energy points above / below (below / above) the Fermi levels⁴⁰, and ϵ_F refers to the default Fermi

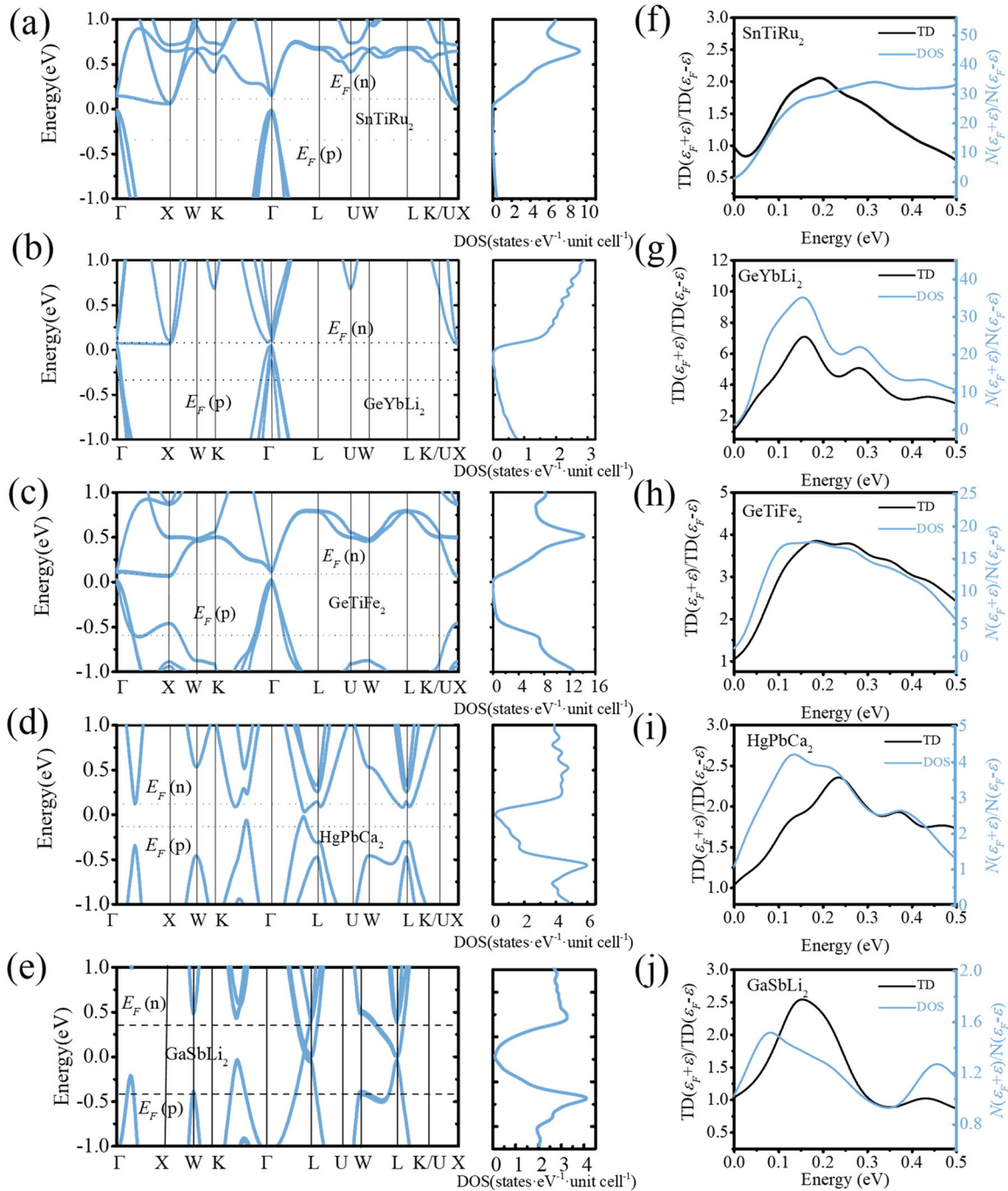


Fig. 4 Electronic structures of five screened systems. The band structures and density of states for **a** SnTiRu₂ **b** GeYbLi₂ **c** GeTiFe₂ **d** HgPbCa₂ **e** GaSbLi₂ and the asymmetry ratio of TD and density of states DOS for **f** SnTiRu₂ **g** GeYbLi₂ **h** GeTiFe₂ **i** HgPbCa₂ **j** GaSbLi₂, with $\epsilon_F + \epsilon$ and $\epsilon_F - \epsilon$ representing the physical quantities above and below the Fermi energy level, respectively. The dashed lines in each band structure represent the positions of the Fermi energy levels for both p-type and n-type PF_{max} .

energy level. As can be found in Fig. 4(f)–(i), the maximum $N(\epsilon_F + \epsilon)/N(\epsilon_F - \epsilon)$ are from 4 to above 30. For SnTiRu₂, GeTiFe₂, and GeYbLi₂, the large DOS of CBM come from the flat band along Γ -X with a large effective mass. Further wave function analyses in Supplementary Fig. 2 indicate that the flat band is caused by the localized *d* orbitals from transition metal elements Ru, Fe, and Yb. For HgPbCa₂, the difference in DOS mainly comes from the additional pocket at L around CBM. When considering the contribution from group velocity, the asymmetry ratio for transport distribution function (TD)³⁷ for the above four compounds is greatly reduced (Fig. 4(f)–(i)) due to the relatively small group velocity for heavy bands, though the TD for the

conduction band is still larger than that for the valence band. The asymmetry of the band-related quantities causes better n-type PF_{max} than the p-type in these four compounds, as shown in Table 1.

Besides the band asymmetry, other physical quantities are also necessary for high PF_{max} . As shown in Eq. 6, small deformation potentials and large Young's moduli are responsible for high electronic relaxation times and power factors. As shown in Table 1, SnTiRu₂ and GeTiFe₂ possess small deformation potentials, at least for the favorable carrier type (lower than 2 eV). And their Young's moduli are ultra-high, around 300 GPa, indicating the stiffness of the two compounds. The two factors ensure the PF_{max} of the two larger

than $200 \times 10^{-4} \text{ W mK}^{-2}$. For GaSbLi₂, due to the fact that bands at both sides of the Fermi level are very dispersive (Fig. 4e), the p-type and n-type group velocities are both high (Table 1). Given the pseudogap at the Fermi level, the large group velocities result in large PF_{max} s for both p-type and n-type in this compound, though the band asymmetry is not large (Fig. 4j).

In conclusion, based on the MatHub-3d, a high-throughput workflow was carried out to find active Peltier cooling Heusler systems with large κ_{eff} . By calculating the electronic structure, electrical transport, and lattice thermal conductivity, five alloys of full-Heusler systems that meet the requirements were finally screened out, namely GaSbLi₂, HgPbCa₂, SnTiRu₂, GeYbLi₂, GeTiFe₂. These five systems have both high electrical conductivity and/or Seebeck coefficient for high active Peltier cooling. The electrical conductivities are high due to the narrow band-gap or gapless electronic structures, as well as very high group velocity as shown in GaSbLi₂. For materials with high Seebeck coefficient, such as HgPbCa₂, SnTiRu₂, GeYbLi₂, GeTiFe₂, their heavier conduction bands ensure the band asymmetry. This work demonstrates that the active thermal conductivity κ_{ac} induced by PF is the most important component of active Peltier cooling at small temperature differences relative to the passive thermal conductivity κ_{pas} .

METHODS

All first-principles calculations in the work were based on Vienna ab initio Simulation Package with the projector augmented wave method implemented^{41,42}. For the calculations of the electronic structures, the Strongly Constrained and Appropriately Normed (SCAN)⁴³ semilocal density functional was used throughout the work. Plane-wave energy cutoff energy of 520 eV and energy convergence criterion of 10^{-4} eV for self-consistent were adopted for all the calculations, the k-grid used in the calculation of the self-consistent calculation is $60/L+1$, where L is the lattice constant of the systems. For the systems with magnetic properties, we considered the ferromagnetic ordering and did not further consider possible antiferromagnetic ordering. Moreover, the five systems we screened were all non-magnetic. Supplementary Table 2 lists the VASP pseudopotential names adopted for the lanthanide elements in this work. TransOpt⁴⁴ was used for the electrical transport properties, the k-grid used in the calculation of the transport properties is $240/L+1$. The electrical conductivity σ , Seebeck coefficient S , and electronic thermal conductivity κ_e were written using the Levi-Civita symbol,

$$\sigma_{\alpha\beta}(\mu, T) = \frac{1}{V} \sum_{nk} \mathbf{v}_{nk\alpha} \mathbf{v}_{nk\beta} \tau_{nk} \left[-\frac{\partial f_{\mu}(\epsilon_{nk}, T)}{\partial \epsilon_{nk}} \right], \quad (2)$$

$$S_{\alpha\beta}(\mu, T) = \frac{1}{eTV} \sigma_{\alpha\beta}(\mu, T)^{-1} \sum_{nk} \mathbf{v}_{nk\alpha} \mathbf{v}_{nk\beta} \tau_{nk} (\mu - \epsilon_{nk}) \left[-\frac{\partial f_{\mu}(\epsilon_{nk}, T)}{\partial \epsilon_{nk}} \right], \quad (3)$$

$$\begin{aligned} \kappa_{e\alpha\beta}(\mu, T) &= \frac{1}{e^2TV} \sum_{nk} \mathbf{v}_{nk\alpha} \mathbf{v}_{nk\beta} \tau_{nk} (\mu - \epsilon_{nk})^2 \left[-\frac{\partial f_{\mu}(\epsilon_{nk}, T)}{\partial \epsilon_{nk}} \right] \\ &\quad - \frac{1}{eV} \sum_{nk} \mathbf{v}_{nk\alpha} \mathbf{v}_{nk\beta} \tau_{nk} (\mu - \epsilon_{nk}) \left[-\frac{\partial f_{\mu}(\epsilon_{nk}, T)}{\partial \epsilon_{nk}} \right] S_{\gamma\beta}(\mu, T), \end{aligned} \quad (4)$$

here v_{nk} is electron group velocity corresponding to band index n and reciprocal coordinate \mathbf{k} , and τ_{nk} is electronic relaxation time. T , μ , V , f_{μ} , e , and ϵ_{nk} are respectively absolute temperature, Fermi level, volume of unit cell, the Fermi-Dirac distribution, electron charge, and band energy. The electron group velocity corresponding to energy μ is calculated as shown in Eq. 5,

$$v_e(\mu, T) = \frac{\sqrt{\sum_{nk} (\mathbf{v}_{nkx}^2 + \mathbf{v}_{nky}^2 + \mathbf{v}_{nkz}^2) \left[-\frac{\partial f_{\mu}(\epsilon_{nk}, T)}{\partial \epsilon_{nk}} \right]}}{\sum_{nk} \left[-\frac{\partial f_{\mu}(\epsilon_{nk}, T)}{\partial \epsilon_{nk}} \right]}. \quad (5)$$

It is notable that v_e is the average of each anisotropic electron group velocity v_{kx} , v_{ky} , and v_{kz} . In order to balance the efficiency and accuracy in the HTP study, the method of constant electron–phonon coupling approximation (CEPCA) combined with deformation potential method were adopted,

$$\frac{1}{\tau_{nk}} = \frac{2\pi k_B T E_{def}^2}{V \hbar G} \sum_{mk'} \delta(\epsilon_{nk} - \epsilon_{mk'}), \quad (6)$$

where n and \mathbf{k} are the band index and wave vector, E_{def} is the deformation potential of the band edge, G is the Young's modulus, and $\delta(\epsilon_{nk} - \epsilon_{mk'})$ takes the form of Gaussian function. For the calculation of the deformation potential, the average value of the first energy band was used as the reference level. In this work, the deformation potentials for the VBM and CBM were considered separately.

The Slack model was adopted to obtain the lattice thermal conductivity^{45–47},

$$\kappa_L = A \frac{\bar{m} V_m^{\frac{1}{3}} v_q^3}{n^{\frac{2}{3}} \gamma^2 T}, \quad (7)$$

where \bar{m} is the average atomic mass, v_q is sound velocity, V_m is the atomic volume, n is the number of atoms in the original cell, γ is the Gruneisen constant, and A is the quantity related to γ , respectively. Here, the Gruneisen constant and the mean sound velocity are related to the elastic matrices c_{ij} , which are calculated by the home-made elastic property automated calculation code (EPAC)^{39,48}. The detailed formulas can be found in the supplemental material.

DATA AVAILABILITY

The data that support the findings of this study are available from the corresponding author upon reasonable request.

CODE AVAILABILITY

The calculations of the electrical transport properties in this work rely heavily on TransOpt³⁶. The code of TransOpt is available at <https://github.com/yangjio4849/TransOpt>. All the home-made codes used to generate the data is available from the corresponding author upon reasonable request.

Received: 4 April 2022; Accepted: 4 September 2022;
Published online: 17 September 2022

REFERENCES

- Domke, K. & Skrzypczak, A. Peltier modules in cooling system for electronic components. *WIT trans. Eng. Sci.* **68**, 3–12 (2010).
- Wijngaards, D. & Wolffenbuttel, R. F. Study on temperature stability improvement of on-chip reference elements using integrated Peltier coolers. *IEEE Trans. Instrum. Meas.* **52**, 478–482 (2003).
- Kim, J., Oh, J. & Lee, H. Review on battery thermal management system for electric vehicles. *Appl. Therm. Eng.* **149**, 192–212 (2019).
- Maruyama, S., Komiya, A., Takeda, H. & Aiba, S. Development of precise-temperature-controlled cooling apparatus for medical application by using Peltier effect. *Int. Conf. Biomed. Eng. Inf.* **2**, 610–614 (2008).
- Pop, E., Sinha, S. & Goodson, K. E. Heat generation and transport in nanometer-scale transistors. *Proc. IEEE* **94**, 1587–1601 (2006).
- Shakouri, A. Nanoscale thermal transport and microrefrigerators on a chip. *Proc. IEEE* **94**, 1613–1638 (2006).
- Nimmagadda, L. A. & Sinha, S. Thermoelectric property requirements for on-chip cooling of device transients. *IEEE Trans. Electron Dev.* **67**, 3716–3721 (2020).
- Adams, M. J., Verosky, M., Zebarjadi, M. & Heremans, J. P. Active Peltier coolers based on correlated and Magnon-Drage metals. *Phys. Rev. Appl.* **11**, 054008 (2019).
- Zebarjadi, M. Electronic cooling using thermoelectric devices. *Appl. Phys. Lett.* **106**, 203506 (2015).
- Mao, J., Chen, G. & Ren, Z. Thermoelectric cooling materials. *Nat. Mater.* **20**, 454–461 (2021).

11. Smith, L. J. B., Corbin, S. F., Hexemer, R. L., Donaldson, I. W. & Bishop, D. P. Development and processing of novel aluminum powder metallurgy materials for heat sink applications. *Metall. Mater. Trans. A* **45**, 980–989 (2014).
12. Hanumanthappa, R., Dassappa, S. & Ananda, G. K. Thermal analysis on heat sink made up of aluminium alloys with copper compositions. *Mater. Today.: Proc.* **42**, 493–499 (2020).
13. Zhao, W. et al. Enhanced thermoelectric performance in barium and indium double-filled Skutterudite Bulk materials via orbital hybridization induced by indium filler. *J. Am. Chem. Soc.* **131**, 3713–3720 (2009).
14. Shi, X. et al. Multiple-filled skutterudites: high thermoelectric figure of merit through separately optimizing electrical and thermal transports. *J. Am. Chem. Soc.* **133**, 7837–7846 (2012).
15. Hsu, K. F. et al. Cubic AgPbmSbTe_{2+m}: Bulk thermoelectric materials with high figure of merit. *Science* **303**, 818–821 (2004).
16. Biswas, K. et al. High-performance bulk thermoelectrics with all-scale hierarchical architectures. *Nature* **489**, 414–418 (2012).
17. Shi, X. et al. Low thermal conductivity and high thermoelectric figure of merit in n-type BaxYbyCo(4)Sb(12) double-filled skutterudites. *Appl. Phys. Lett.* **92**, 182101 (2008).
18. Fang, T. et al. Complex band structures and lattice dynamics of Bi₂Te₃-based compounds and solid solutions. *Adv. Funct. Mater.* **29**, 1900677 (2019).
19. Xu, Z. et al. Attaining high mid-temperature performance in (Bi,Sb)(2)Te-3 thermoelectric materials via synergistic optimization. *NPG Asia Mater.* **8**, e302 (2016).
20. Kim, T. Y., Park, C. H. & Marzari, N. The electronic thermal conductivity of graphene. *Nano Lett.* **16**, 2439–2443 (2016).
21. Markov, M., Rezaei, S. E., Sadeghi, S. N., Esfarjani, K. & Zebarjani, M. Thermoelectric properties of semimetals. *Phys. Rev. Mater.* **3**, 095401 (2019).
22. Yang, J. et al. Evaluation of Half-Heusler compounds as thermoelectric materials based on the calculated electrical transport properties. *Adv. Funct. Mater.* **18**, 2880–2888 (2008).
23. Yu, J., Xia, K., Zhao, X. & Zhu, T. High performance p-type half-Heusler thermoelectric materials. *J. Phys. D.-Appl. Phys.* **51**, 113001 (2018).
24. Zhu, T., Fu, C., Xie, H., Liu, Y. & Zhao, X. High-efficiency Half-Heusler thermoelectric materials for energy harvesting. *Adv. Energy Mater.* **5**, 1500588 (2015).
25. Xia, K. et al. Short-range order in defective half-Heusler thermoelectric crystals. *Energy Environ. Sci.* **12**, 1568–1574 (2019).
26. Xia, K., Hu, C., Fu, C., Zhao, X. & Zhu, T. Half-Heusler thermoelectric materials. *Appl. Phys. Lett.* **118**, 140503 (2021).
27. Qiu, P., Yang, J., Huang, X., Chen, X. & Chen, L. Effect of antisite defects on band structure and thermoelectric performance of ZrNiSn half-Heusler alloys. *Appl. Phys. Lett.* **96**, 152105 (2010).
28. Nishino, Y., Deguchi, S. & Mizutani, U. Thermal and transport properties of the Heusler-type Fe₂VAl_{1-x}Gex (0 < x <= 0.20) alloys: Effect of doping on lattice thermal conductivity, electrical resistivity, and Seebeck coefficient. *Phys. Rev. B* **74**, 6 (2006).
29. Garmroudi, F. et al. Solubility limit and annealing effects on the microstructure & thermoelectric properties of Fe₂V_{1-x}TaxAl_{1-y}Si_y Heusler compounds. *Acta Mater.* **212**, 9 (2021).
30. Garmroudi, F. et al. Boosting the thermoelectric performance of Fe₂VAl-type Heusler compounds by band engineering. *Phys. Rev. B* **103**, 14 (2021).
31. Parzer, M. et al. High solubility of Al and enhanced thermoelectric performance due to resonant states in Fe₂VAl_x. *Appl. Phys. Lett.* **120**, 7 (2022).
32. MatHub-3d. <http://www.mathub3d.net>.
33. Yao, M. et al. Materials informatics platform with three-dimensional structures, workflow and thermoelectric applications. *Sci. Data* **8**, 236 (2021).
34. Li, X. et al. Defect-mediated Rashba engineering for optimizing electrical transport in thermoelectric BiTe. *npj Comput. Mater.* **6**, 107 (2020).
35. Ioffe A. F. Semiconductor Thermoelements and Thermoelectric Cooling. *Information Limited, London* (1957).
36. Yang, J. et al. Power factor enhancement in light valence band p-type skutterudites. *Appl. Phys. Lett.* **101**, 022101 (2012).
37. Xi, L. et al. Discovery of high-performance thermoelectric chalcogenides through reliable high-throughput material screening. *J. Am. Chem. Soc.* **140**, 10785–10793 (2018).
38. Zuo, Q. et al. Thermal conductivity of the diamond-Cu composites with chromium addition. *Adv. Mater. Res.* **311–313**, 287–292 (2011).
39. Cao, Y. et al. Unraveling the relationships between chemical bonding and thermoelectric properties: n-type ABO₃ perovskites. *J. Mater. Chem. A* **10**, 11039–11045 (2022).
40. Chasapis, T. C. et al. Two-band model interpretation of the p- to n-transition in ternary tetradymite topological insulators. *APL Mater.* **3**, 8 (2015).
41. Kresse, G. & Furthmüller, J. Efficient iterative schemes for ab initio total-energy calculations using a plane-wave basis set. *Phys. Rev. B* **54**, 11169–11186 (1996).
42. Blochl, P. E. Projector augmented-wave method. *Phys. Rev. B Condens. Matter* **50**, 17953–17979 (1994).
43. Sun, J., Ruzsinszky, A. & Perdew, J. P. Strongly constrained and appropriately normed semilocal density functional. *Phys. Rev. Lett.* **115**, 036402 (2015).
44. Li, X. et al. TransOpt. A code to solve electrical transport properties of semiconductors in constant electron-phonon coupling approximation. *Comput. Mater. Sci.* **186**, 110074 (2021).
45. Slack, G. A. Nonmetallic crystals with high thermal conductivity. *J. Phys. Chem. Solids* **34**, 321–335 (1973).
46. Jia, T., Chen, G. & Zhang, Y. Lattice thermal conductivity evaluated using elastic properties. *Phys. Rev. B* **95**, 155206 (2017).
47. Li, R. et al. High-throughput screening for advanced thermoelectric materials: diamond-like ABX₂ compounds. *ACS Appl. Mater. Interfaces* **11**, 24859–24866 (2019).
48. Sun, L., Liu, B., Wang, J., Li, Z. & Wang, J. Theoretical study on the relationship between crystal chemistry and properties of quaternary Y-Si-O-N oxynitrides. *J. Am. Ceram. Soc.* **99**, 2442–2450 (2016).

ACKNOWLEDGEMENTS

This work is supported by the Key Research Project of Zhejiang Lab (No. 2021PE0AC02), the National Key Research and Development Program of China (No. 2018YFB0703600), and the Natural Science Foundation of China (Grant nos. 52172216 and 92163212). Part of the computing resources are supported by the Center for Computational Science and Engineering at Southern University of Science and Technology.

AUTHOR CONTRIBUTIONS

The initial idea was developed by J.Y. and X.L. Data from MatHub-3d, calculated by Y.W. H.L. performed the high-throughput calculations. All authors participated in the data analysis, writing, and reading the paper. J.Y. managed the project.

COMPETING INTERESTS

The authors declare no competing interests.

ADDITIONAL INFORMATION

Supplementary information The online version contains supplementary material available at <https://doi.org/10.1038/s41524-022-00887-4>.

Correspondence and requests for materials should be addressed to Xin Li or Jiong Yang.

Reprints and permission information is available at <http://www.nature.com/reprints>

Publisher's note Springer Nature remains neutral with regard to jurisdictional claims in published maps and institutional affiliations.



Open Access This article is licensed under a Creative Commons

Attribution 4.0 International License, which permits use, sharing, adaptation, distribution and reproduction in any medium or format, as long as you give appropriate credit to the original author(s) and the source, provide a link to the Creative Commons license, and indicate if changes were made. The images or other third party material in this article are included in the article's Creative Commons license, unless indicated otherwise in a credit line to the material. If material is not included in the article's Creative Commons license and your intended use is not permitted by statutory regulation or exceeds the permitted use, you will need to obtain permission directly from the copyright holder. To view a copy of this license, visit <http://creativecommons.org/licenses/by/4.0/>.

© The Author(s) 2022